

Levenberg-Marquardt algorithm for acousto-electric tomography based on the complete electrode model

Changyou Li^a, Mirza Karamehmedović^b, Ekaterina Sherina^c, Kim Knudsen^b

^a*School of Information and Electronics, Northwestern Polytechnical University*

^b*Department of Applied Mathematics and Computer Science, Technical University of Denmark*

^c*Department of Mathematics, University of Vienna*

Abstract

The inverse problem in Acousto-Electric tomography concerns the reconstruction of the electric conductivity in a domain from knowledge of the power density function in the interior of the body. This interior power density results from currents prescribed at boundary electrodes (and can be obtained through electrostatic boundary measurements together with auxiliary acoustic measurement). In Electrical Impedance Tomography the complete electrode model is known to be the most accurate model for the forward modelling.

In this paper the reconstruction problem of Acousto-Electric tomography is posed using the (smooth) complete electrode model, and a Levenberg-Marquardt iteration is formulated in appropriate function spaces. This results in a system of partial differential equations to be solved in each iteration. To increase the computational efficiency and stability, a strategy based on both the complete electrode model and the continuum model with Dirichlet boundary condition is proposed.

The system of equations is implemented numerically for a two dimensional scenario and the algorithm is tested on two different numerical phantoms, a heart and lung model and a human brain model. Several numerical experiments are carried out confirming the feasibility, accuracy and stability of the methods.

Keywords: Acousto-electric tomography, Electrical impedance tomography, Complete electrode model, Continuum model, Levenberg-Marquardt algorithm

2010 MSC: 65J22, 35R30, 65M32

1. Introduction

Electrical Impedance Tomography (EIT) is an emerging technology for obtaining the internal conductivity of a physical body from boundary measurements of currents or voltages on the surface of the body [1–3]. It is an ill-posed problem due to the fact that boundary measurements show little sensitive to (even large) changes of interior conductivity distribution [4]. Intensive research exists on this topic [5, 6]; many regularization methods have been proposed to overcome the ill-posedness and to improve the imaging quality [7–10].

More recently it has been suggested to augment the measurement setup in EIT with an ultra-sonic device thus yielding the hybrid imaging method known as Acousto-Electric tomography (AET) [11]. The resulting modality has been investigated theoretically and numerically, and AET seems to have the potential to dramatically increase the contrast, resolution, and stability of the conductivity reconstruction [12, 13].

The idea of AET it is to conduct a usual EIT experiment while a known focused ultrasonic wave travels through the object. The high intensity of the acoustic pressure will create a small local deformation in the physical body and thus of the electrical conductivity due to the acousto-electric effect [14].

A physical body imaged by EIT is modeled as a bounded Lipschitz domain $\Omega \subset \mathbb{R}^n$ for $n \geq 2$. The changes caused by the acoustic wave can be recorded by EIT measurements on the boundary $\partial\Omega$ [15, 16]. The power density in Ω is then

$$\mathcal{E}(\sigma) = \sigma |\nabla u(\sigma)|^2. \quad (1)$$

Here, $\sigma \geq c > 0$ is the conductivity and $u(\sigma)$ is the electrical potential inside Ω produced by applying an electric field on the boundary $\partial\Omega$. We call \mathcal{E} the power density operator. With the assumption that measurements are carried out in low temporal frequency and that Ω contains no interior sources or sinks of charges the governing equation is the generalized Laplace equation

$$\nabla \cdot \sigma \nabla u = 0 \quad \text{in } \Omega \quad (2)$$

subject to suitable boundary conditions. Given noisy measurements \mathcal{E}^δ of the true power densities $\mathcal{E}(\sigma)$ the problem is to reconstruct σ . We approach the problem by optimization

$$\min_{\sigma} \|\mathcal{E}^\delta - \mathcal{E}(\sigma)\|_{L^2(\Omega)}. \quad (3)$$

In AET the power density $\mathcal{E}(\sigma)$ can be computed from the boundary measurements [4, 13, 17]. The nonlinear relationship between $\mathcal{E}(\sigma)$ and σ renders the problem nonlinear [18]. Some methods have been developed in the literature for reconstructing σ from $\mathcal{E}(\sigma)$ [4, 11–13, 18–20], but all these methods are based on the continuum model with Dirichlet or Neumann boundary conditions. See also [21–24] for optimization approaches to the problem different from (3). The limited data problem was considered in [25].

The Complete Electrode Model (CEM) is a practical model for EIT, and it can simulate the electrical potential with a very good accuracy [26]. In the model, L electrodes are attached on boundary $\partial\Omega$. A known total current I_l injected through the l -th electrode e_l is given as

$$\int_{e_l} \sigma \frac{\partial u}{\partial \nu} = I_l, \quad l = 1, \dots, L. \quad (4)$$

Here, ν is the outward unit normal vector to the boundary $\partial\Omega$. e_l is the l -th electrode, and $\partial/\partial\nu$ indicates the derivative of u in the direction of the outward unit normal vector ν . Since there is no current flowing out through boundary regions without electrodes, one has

$$\sigma \frac{\partial u}{\partial \nu} = 0 \quad \text{on } \partial\Omega \setminus \bigcup_{l=1}^L e_l. \quad (5)$$

On the electrode e_l the electric potential U_l is assumed to be constant. This boundary potential consist of a part due to the interior potential u and a part due to the electrode contact, and it is comprised in the model

$$u + z_l \sigma \frac{\partial u}{\partial \nu} = U_l \quad \text{on } e_l \quad (6)$$

where z_l denotes the so-called contact impedance assumed to be constant on the l -th electrode. The partial differential equation (2) with boundary conditions (4)-(6) gives the CEM. To ensure existence and uniqueness of the solution, this model also needs to include the law of charge conservation

$$\sum_{l=1}^L I_l = 0 \quad (7)$$

and to determine the potential's grounding by

$$\sum_{l=1}^L U_l = 0. \quad (8)$$

The CEM problem (2)-(6) has a unique solution $u \in H^{2-\epsilon}(\Omega)$ for any $\epsilon > 0$ [27], however the mixed boundary conditions (5)-(6) allow singularities near the edges of the electrodes. In order to increase the regularity of u the electrode conductance $\zeta_l = 1/z_l$ is introduced as a function

$$\nabla \cdot \sigma \nabla u = 0 \quad \text{in } \Omega, \quad (9a)$$

$$\sigma \frac{\partial u}{\partial \nu} = \zeta(U_l - u) \quad \text{on } e_l, \quad (9b)$$

$$\int_{e_l} \sigma \frac{\partial u}{\partial \nu} = I_l \quad \text{on } e_l. \quad (9c)$$

Assuming that $\zeta_l \in H^t(\partial\Omega)$ for some $t > (n-1)/2$ then $u(\sigma) \in H^{t+\frac{3}{2}}(\Omega)$ [27]. In particular for $t = s > n/2$, $u(\sigma) \in H^{s+1}(\Omega)$ and $\mathcal{E}(\sigma) \in H^s(\Omega)$. We call (9) the smoothed CEM (SCEM).

The main aim of this paper is to develop an iterative method for reconstructing σ from $\mathcal{E}^\delta(\sigma)$. Inspired by [12] the method will be based on the Levenberg-Marquardt method for solving the least squares problem (3). The main novelty here being the use of the SCEM to accurately and stably model electrodes and the electric current in the forward problem. In addition, a reconstruction strategy based on a combined use of both CEM and Continuum model with Dirichlet boundary condition (DCM) is proposed to increase the computational efficiency.

The outline of the paper is as follows. In Section 2, the Levenberg-Marquardt method is briefly introduced. The non-linear problem is linearized, and the adjoint problem is setup. In Section 3, the iterative reconstruction method is developed based on CEM and Levenberg-Marquardt iteration. A linear system is built to calculate the updating step for each iteration. The algorithm for increasing efficiency by exploiting DCM is also introduced in this section. These algorithms are implemented and applied to reconstruct the conductivity distribution of several phantoms in Section 4, numerical performances of different algorithms are discussed in detail. The conclusion of the presented work is given in Section 5.

2. Reconstruction algorithm

In this section we will first recap the Levenberg-Marquardt Algorithm for solving (non-linear) optimization problems. Then we will for the particular problem in AET with CEM derive the necessary ingredients, that is the Fréchet derivative of \mathcal{E} and its adjoint.

2.1. The Levenberg-Marquardt Algorithm

Let $F : X \rightarrow Y$ be a (possibly non-linear) operator between Hilbert spaces X and Y . For some $y^\delta = y + \delta \in Y$ with $y \in \text{Ran}(F)$ the problem is to solve at least approximately the equation $F(\sigma) \approx y^\delta$, and often the minimization problem

$$\arg \min_{\sigma \in X} \|F(\sigma) - y^\delta\|_Y^2 \quad (10)$$

is considered. If F is (Fréchet) differentiable, the linear approximation

$$F(\sigma) - F(\sigma_k) \approx F'(\sigma_k)(\sigma - \sigma_k)$$

yields the iterative scheme

$$\sigma_{k+1} = \arg \min_{\sigma} \|y^\delta - F(\sigma_k) - F'(\sigma_k)(\sigma - \sigma_k)\|_Y^2$$

solved by the Newton algorithm

$$\sigma_{k+1} = \sigma_k + F'(\sigma_k)^{-1}(y^\delta - F(\sigma_k)).$$

This is applicable only when $F'(\sigma_k)$ is left-invertible. In general one can instead minimize the following Tikhonov functional [28]

$$\sigma_{k+1} = \arg \min_{\sigma} \|y^\delta - F(\sigma_k) - F'(\sigma_k)(\sigma - \sigma_k)\|_Y^2 + \alpha_k \|\sigma - \sigma_k\|_X^2, \quad (11)$$

where $\alpha_k > 0$ is the regularization parameter; this minimization problem is solved by the Levenberg-Marquardt Algorithm (LMA)

$$\sigma_{k+1} = \sigma_k + (F'(\sigma_k)^* F'(\sigma_k) + \alpha_k Id)^{-1} F'(\sigma_k)^*(y^\delta - F(\sigma_k)). \quad (12)$$

Here, $F'(\sigma_k)^*$ is the adjoint of $F'(\sigma_k)$ and Id is identity operator. When the operator F satisfies a certain non-linearity condition, a proper choice of the parameter α_k and the initial guess σ_0 sufficiently close to the desired solution, the LMA converges to a solution σ^δ of (10).

The LMA can be thought of as a combination of steepest descent and Gauss-Newton method. When the current solution is far from the correct one, a large value is assigned to $\alpha_k > 0$, and LMA behaves like a steepest-descent method which converges slowly. When the current solution is close to the correct solution, a small $\alpha_k > 0$ is used, and LMA behaves like a Gauss-Newton method, which has faster convergence.

2.2. The Fréchet derivative \mathcal{E}' and its adjoint

In the present work we consider the operator $F(\sigma) = \mathcal{E}(\sigma)$ in (1). In order to apply (12) we therefore need to calculate the Fréchet derivative $\mathcal{E}'(\sigma)$ of the power density operator at σ and its adjoint $\mathcal{E}'(\sigma)^*$.

We start with the Fréchet derivative of $u(\sigma)$, i.e. the operator $u'(\sigma) : H^s(\Omega) \rightarrow H^{s+1}(\Omega)$. The Fréchet derivative can be calculated (see the general approach in [29]) in the following way: For a given $\tau \in H^s(\Omega)$ with compact support inside Ω the difference $u(\sigma + \tau) - u(\sigma)$ is approximated by a function $\xi = u'(\sigma)\tau$ that is linear in τ . Indeed, define $(\xi, \Xi) \in H^{s+1}(\Omega) \times \mathbb{R}^n$ as the solution to the modified CEM problem

$$\nabla \cdot \sigma \nabla \xi + \nabla \cdot (\tau \nabla u(\sigma)) = 0 \quad \text{in } \Omega, \quad (13a)$$

$$\sigma \frac{\partial \xi}{\partial \nu} = \zeta(\Xi_l - \xi) \quad \text{on } e_l, \quad (13b)$$

$$\int_{e_l} \sigma \frac{\partial \xi}{\partial \nu} = 0 \quad \text{on } e_l. \quad (13c)$$

With the grounding $\sum \Xi_l = 0$, (13) has a unique weak solution $\xi \in H^{s+1}(\Omega)$, $\Xi \in \mathbb{R}^n$, which obviously is linear with respect to τ . Moreover,

$$\|u(\sigma + \tau) - u(\sigma) - \xi\|_{H^{s+1}(\Omega)} \leq C \|\tau\|_{H^s(\Omega)}$$

showing that $\xi = u'(\sigma)\tau$ is indeed the Fréchet derivative of u at σ

The Fréchet derivative $\mathcal{E}(\sigma)\tau$ of $\mathcal{E}(\sigma)$ in the direction τ is obtained as in [20] by

$$\mathcal{E}(\sigma + \tau) - \mathcal{E}(\sigma) \approx \mathcal{E}'(\sigma)\tau = \tau |\nabla u(\sigma)|^2 + 2\sigma \nabla u(\sigma) \cdot \nabla u'(\sigma)\tau \quad (14)$$

We now compute the adjoint $(\mathcal{E}'(\sigma))^*$ first as an operator in $L^2(\Omega)$: Consider for some $z \in L^2(\Omega)$

$$\langle z, \mathcal{E}'(\sigma)\tau \rangle_{L^2(\Omega)} = \int z (\tau |\nabla u(\sigma)|^2 + 2\sigma \nabla u(\sigma) \cdot \nabla u'(\sigma)\tau) dx. \quad (15)$$

We focus on the second part of the integral (the first part is self-adjoint). Introduce the pair $v(z) \in H^1(\Omega)$ and $V \in \mathbb{R}^n$ defined by the weak PDE form (for all w, W)

$$\int_{\Omega} \sigma \nabla v(z) \cdot \nabla w dx + \sum_l \int_{\partial\Omega} \zeta(V_l(z) - v(z))(W_l - w) dS = \int_{\Omega} 2\sigma z \nabla u(\sigma) \cdot \nabla w dx. \quad (16)$$

The strong form reads

$$\begin{aligned} \nabla \cdot \sigma \nabla v &= 2\nabla \cdot \sigma z \nabla u(\sigma), \\ \sigma \frac{\partial v}{\partial \nu} &= \zeta(V_l - v) \quad \text{on } e_l, \\ \int_{e_l} \sigma \frac{\partial v}{\partial \nu} dS &= 0, \\ \sigma \frac{\partial v}{\partial \nu} &= 0 \quad \text{outside } e_l. \end{aligned}$$

Then insert the choice $(w, W) = (\xi, \Xi)$ in (16) to calculate the latter term in the RHS of (15)

$$\begin{aligned} \int_{\Omega} 2z \sigma \nabla u(\sigma) \cdot \nabla \xi dx &= \int_{\Omega} \sigma \nabla v(z) \cdot \xi dx + \sum_l \int_{\partial\Omega} \zeta(V_l(z) - v(z))(\Xi_l - \xi) dS \\ &= - \int_{\Omega} \tau \nabla u(\sigma) \cdot \nabla v(z) dx, \end{aligned}$$

where the last equality follows from the weak form of (13). Thus we find the form

$$\begin{aligned} \langle (\mathcal{E}'(\sigma))^* z, \tau \rangle_{L^2(\Omega)} &= \langle z, \mathcal{E}'(\sigma) \tau \rangle_{L^2(\Omega)} \\ &= \langle |\nabla u(\sigma)|^2 z - \nabla u(\sigma) \cdot \nabla v(z), \tau \rangle_{L^2(\Omega)}, \end{aligned}$$

that is

$$(\mathcal{E}'(\sigma))^* z = |\nabla u(\sigma)|^2 z - \nabla u(\sigma) \cdot \nabla v(z). \quad (17)$$

To get to the adjoint in higher order Sobolev spaces $H^s(\Omega)$ for the chosen $s > n/2$ (e.g. $s = 2$ in 2D) we lift the operator to higher order spaces, i.e. we solve for $x \in H^s(\Omega)$

$$\langle x, \tau \rangle_{H^s(\Omega)} = \langle (\mathcal{E}'(\sigma))^* z, \tau \rangle_{L^2(\Omega)}.$$

This is a fourth order PDE problem when $s = 2$. With an embedding operator $B : H^2(\Omega) \rightarrow L^2(\Omega)$, $\mathcal{E}'(\sigma)^*$ can be written for $z \in L^2(\Omega)$ as

$$\mathcal{E}'(\sigma)^* : L^2(\Omega) \rightarrow H^2(\Omega) \quad (18)$$

$$\mathcal{E}'(\sigma)^* z = B^* \tilde{\mathcal{E}}'(\sigma)^* z \quad (19)$$

where $\tilde{\mathcal{E}}'(\sigma)^*$ is the $L^2(\Omega)$ -adjoint of $\mathcal{E}'(\sigma)$.

We now restrict ourselves to $n = 2$, i.e. $\Omega \subset \mathbb{R}^2$, and consider the presence of noise. Since noise can not be assumed to be differentiable $\mathcal{E}(\sigma) : H^2(\Omega) \rightarrow L^2(\Omega)$. Since $\mathcal{E}'(\sigma) : H^2(\Omega) \rightarrow L^2(\Omega)$ is a bounded operator, its Hilbert adjoint $\mathcal{E}'(\sigma)^* : L^2(\Omega) \rightarrow H^2(\Omega)$ is bounded as well [30]. With an embedding operator $B : H^2(\Omega) \rightarrow L^2(\Omega)$, $\mathcal{E}'(\sigma)^*$ can be written as

$$\mathcal{E}'(\sigma)^* : L^2(\Omega) \rightarrow H^2(\Omega) \quad (20)$$

$$\mathcal{E}'(\sigma)^* z = B^* \tilde{\mathcal{E}}'(\sigma)^* z \quad (21)$$

where $\tilde{\mathcal{E}}'(\sigma)^*$ is the $L^2(\Omega)$ -adjoint of $\mathcal{E}'(\sigma)$. $z \in L^2(\Omega)$.

Instead of directly calculating $\mathcal{E}'(\sigma)^*$ in $H^2(\Omega)$, the form of $\tilde{\mathcal{E}}'(\sigma)^*$ in $L^2(\Omega)$ is firstly found, which is given as

$$\tilde{\mathcal{E}}'(\sigma)^* : L^2(\Omega) \rightarrow L^2(\Omega) \quad (22)$$

$$\tilde{\mathcal{E}}'(\sigma)^* z = |\nabla u(\sigma)|^2 z + 2\nabla u \nabla V z. \quad (23)$$

Here, $V = V(\sigma, u(\sigma))$ with $V : H^2(\Omega) \rightarrow H^2(\Omega)$ be a linear operator defined by

$$L_\sigma V z = -\nabla \cdot (z \sigma \nabla u(\sigma)) \quad \text{in } \Omega, \quad (24a)$$

$$\sigma \frac{\partial V z}{\partial \nu} = \zeta(V_i - V z) \quad \text{on } e_i, \quad (24b)$$

$$\int_{e_i} \sigma \frac{\partial V z}{\partial \nu} = 0 \quad \text{on } e_i, \quad (24c)$$

$$\sigma \frac{\partial V z}{\partial \nu} = 0 \quad \text{off } e_i \quad (24d)$$

3. Iterative reconstruction algorithm based on LMA

According to the Levenberg-Marquardt iteration given in (12), the formulation for calculating the k -th updating step τ_k for the presented problem is explicitly given as

$$(\mathcal{E}'(\sigma_k))^* \mathcal{E}'(\sigma_k) + \alpha_k Id \tau_k = \mathcal{E}'(\sigma_k)^* (\mathcal{E}^\delta - \mathcal{E}(\sigma_k)). \quad (25)$$

$\mathcal{E}'(\sigma_k)^* \mathcal{E}'(\sigma_k) \tau = B^* M \tau$ with

$$M \tau = |\nabla u|^2 (\tau |\nabla u|^2 + 2\sigma \nabla u \cdot \nabla u'(\sigma) \tau) + 2\nabla u \cdot \nabla V(\tau |\nabla u|^2) + 4\nabla u \cdot \nabla V(\sigma \nabla u \cdot \nabla u'(\sigma) \tau). \quad (26)$$

Here, $M_e \tau$ is easily obtained with (14), (21), and (23). After computing τ_k from (25), the conductivity map σ_k obtained from the k -th iteration is updated by $\sigma_{k+1} = \sigma_k + \tau_k$ for a new iteration. All PDEs are coupled and collected into the PDE system

$$\phi + \alpha_k \tau_k = y, \quad \text{in } \Omega, \quad (27a)$$

$$\Delta \phi - \chi = 0, \quad \text{on } \partial \Omega, \quad (27b)$$

$$\beta^2 \Delta \chi + \phi - \gamma = 0, \quad \text{on } \partial \Omega, \quad (27c)$$

$$\partial \phi / \partial \nu = 0, \quad \text{on } \partial \Omega \quad (27d)$$

$$\partial \chi / \partial \nu = 0, \quad \text{on } \partial \Omega \quad (27e)$$

$$\gamma - |\nabla u|^2 \Phi_\epsilon(\tau |\nabla u|^2 + 2\sigma \nabla u \nabla \xi) + 2\nabla u \nabla \zeta + 4\nabla u \nabla \kappa = 0, \quad \text{in } \Omega, \quad (27f)$$

$$\nabla \cdot \sigma \nabla \xi + \nabla \cdot (\tau \nabla u(\sigma)) = 0, \quad \text{in } \Omega, \quad (27g)$$

$$\sigma \frac{\partial \xi}{\partial \nu} = \zeta(\Xi - \xi), \quad \text{on } e_l, \quad (27h)$$

$$\int_{e_l} \sigma \frac{\partial \xi}{\partial \nu} = 0, \quad \text{on } e_l, \quad (27i)$$

$$\nabla \cdot \sigma \nabla \rho + \nabla \cdot (\tau |\nabla u|^2 \sigma \nabla u(\sigma)) = 0, \quad \text{in } \Omega, \quad (27j)$$

$$\sigma \frac{\partial \rho}{\partial \nu} = \zeta(\varrho_l - \rho) \quad \text{on } e_l, \quad (27k)$$

$$\int_{e_l} \sigma \frac{\partial \rho}{\partial \nu} = 0 \quad \text{on } e_l, \quad (27l)$$

$$\sigma \frac{\partial \rho}{\partial \nu} = 0 \quad \text{off } e_l, \quad (27m)$$

$$\nabla \cdot \sigma \nabla \kappa + \nabla \cdot ((\sigma \nabla u \nabla \xi) \cdot \sigma \nabla u(\sigma)) = 0, \quad \text{in } \Omega, \quad (27n)$$

$$\sigma \frac{\partial \kappa}{\partial \nu} = \zeta(\varkappa_l - \kappa) \quad \text{on } e_l, \quad (27o)$$

$$\int_{e_l} \sigma \frac{\partial \kappa}{\partial \nu} = 0, \quad \text{on } e_l, \quad (27p)$$

$$\sigma \frac{\partial \kappa}{\partial \nu} = 0 \quad \text{off } e_l \quad (27q)$$

with $y = \mathcal{E}'(\sigma_k)^*(\mathcal{E}^\delta - \mathcal{E}(\sigma_k))$, $\phi = B^* M \tau$, $\gamma = M \tau$, $\xi = u'(\sigma) \tau$, $\rho = V(\tau |\nabla u|^2)$, and $\kappa = V(\sigma \nabla u \cdot \nabla u'(\sigma) \tau)$. With the number of measurements $M > 1$, the system is formulated with $y = \mathcal{E}'(\sigma_k)^*(\mathcal{E}^\delta - \mathcal{E}(\sigma_k))$ and $\gamma = \sum_m^M [|\nabla u_m|^2 \Phi_\epsilon(\tau |\nabla u_m|^2 + 2\sigma \nabla u_m \nabla \xi_m) + 2\nabla u_m \nabla \zeta_m + 4\nabla u_m \nabla \kappa_m]$. Since equations (27g)-(27o) need to be solved for each measurement, one additional measurement will need 3 additional partial differential equations.

It may be possible to simplify the above PDE system if the interior potential near the measurement boundary and the measured potential both turn out to converge significantly faster (with the number of iterations of the solution procedure) than the conductivity estimate σ . In this case, we would expect $\xi \approx 0$ and $\Xi \approx 0$ to hold early in the iteration. From (27h), we would then get that the change in the current at any e_l resulting from a change in σ is approximately zero after only a few iterations, and conditions (27h) and (27i) might justifiably be substituted with the much simpler Dirichlet boundary condition $\xi = 0$ on e_l .

The iterative reconstruction method based on the above system is here named as LM-SCEM which is demonstrated in Algorithm 1 for a single measurement. The measured data of \mathcal{E}^δ is simulated with SCEM in this paper. The relative error is given by $\eta = \|\sigma_t - \sigma_r\|_{L_2(\Omega)} / \|\sigma_t\|_{L_2(\Omega)}$, where σ_t and σ_r denotes the true and reconstructed conductivities. The parameter α_k should theoretically be updated according to the value

of τ_k . If $\sigma_k + \tau_k$ leads to a reduction of the relative error in σ_k , α_k is decreased and τ_k is accepted. Otherwise, τ_k is discarded and α_k is increased. Since η can not be determined in practice, a relatively large value is assigned to α_0 in this paper, and α_k is slowly decreased to ensure convergence. The iteration is stopped when the L_2 -norm of τ_k is smaller than a given value or the maximum number of iteration is achieved.

Algorithm 1: The LM-SCEM algorithm for reconstructing the conductivity map from single measurement of power density.

Data: The measured power density \mathcal{E}^δ and an initial guess σ_0
Result: The reconstructed conductivity map σ_r with a relative error η

- 1 N : the maximum number of iterations;
- 2 $\sigma_k \leftarrow \sigma_0$;
- 3 $\alpha_k \leftarrow \alpha_0$;
- 4 $num \leftarrow 1$;
- 5 $norm \leftarrow 1$;
- 6 **while** $norm > \delta$ and $num < N$ **do**
- 7 Update u_k from σ_k with CEM;
- 8 Compute $\mathcal{E}(\sigma_k)$ from u_k ;
- 9 Compute $y = \mathcal{E}'(\sigma_k)^*(\mathcal{E}^\delta - \mathcal{E}(\sigma_k))$ Compute τ_k with the linear system defined by (27);
- 10 $\sigma_k \leftarrow \sigma_k + \tau_k$;
- 11 $norm \leftarrow \|\tau_k\|_{L_2}$;
- 12 $num \leftarrow num + 1$;
- 13 Update α_k ;
- 14 **end**

3.1. The LM-DCM method and the mixed reconstruction algorithm

If DCM is considered instead of SCEM, the system for reconstructing σ can be built by a similar calculation [20]. The resulted system for computing τ_k remains the same as the one for LM-SCEM except that the boundary conditions (27h) and (27i) need to be replaced with $\xi = 0$ on $\partial\Omega$. The computation of τ_k in LM-CEM is actually expensive because of the additional unknowns in Ξ . To obtain a good reconstruction accuracy of LM-SCEM, multiple measurements are usually considered, but the computational efficiency will decrease quickly with the increasing number of measurements. Our investigation on the convergence of boundary potential and the conductivity shows that the boundary potential converges much faster, examples are given in numerical experiments. This is mainly because EIT measurement is not very sensitive to the internal change of the conductivity distribution [4]. This property renders EIT an ill-posed problem, but it will be taken as the foundation here to build a faster reconstruction approach by mixing LM-SCEM and LM-DCM, which is abbreviated by LM-SCEM-DCM.

This mixed reconstruction method is illustrated in Algorithm 2 for a single measurement. Here, $\mathbf{U} = [U_1, U_2, \dots, U_L]$, which is a vector composed of the voltages on the electrodes. The true values \mathbf{U}^t can be measured, which is produced when simulating the power density with CEM, therefore no additional computation is required. The information of \mathbf{U}^t is here exploited to define a stopping criteria for reconstructing the boundary potential u_b with LM-SCEM. With a relative error given by $\eta^b = \frac{\|\mathbf{u}^t - \mathbf{u}^k\|_{l_2}}{\|\mathbf{u}^t\|_{l_2}}$, the value of η^b is checked in each iteration, and LM-SCEM is terminated when an expected relative error η_0^b is achieved. Since the regularity of potentials computed from CEM is not so good on $\partial\Omega$, a smaller region $\Omega' = \{x \mid x \in \Omega, \text{dist}(x, \partial\Omega) > d\}$ is defined with a small d which can “smooth” out the possible irregularity of u close to $\partial\Omega$. The boundary potential u_b is here defined on $\partial\Omega'$ and used for the reconstruction with LM-DCM. The power density in Ω' is firstly reconstructed from u_b . This can be achieved with the method introduced in [4] but will be simulated with DCM here. Because there are no additional unknowns Ξ in LM-DCM, the computation will be more efficient, especially for the computation with multiple measurements. Meanwhile, the conductivity map produced by LM-SCEM is used as the initial guess for LM-DCM. This good initial guess will also help LM-DCM converge faster. Therefore, the mixed reconstruction method can provide a practical and efficient computational model for AET.

Algorithm 2: The LM-CEM-DCM algorithm for reconstructing the conductivity map of a domain Ω from a single measurement of power density.

Data: The measured power density \mathcal{E}^δ and the voltage vector \mathbf{u}^t on electrodes. An initial guess σ_0 and an expected relative error η_0^b for \mathbf{u}^k

Result: The reconstructed conductivity map σ_r with a relative error η

- 1 N_c : the maximum number of iteration for LM-CEM;
- 2 N_d : the maximum number of iteration for LM-DCM;
- 3 $\sigma_k \leftarrow \sigma_0$;
- 4 $num \leftarrow 1$;
- 5 $norm \leftarrow 1$;
- 6 **while** $norm > \delta$ and $num < N_c$ **do**
- 7 Update u_k and \mathbf{u}^k from σ_k with CEM;
- 8 $\eta_b \leftarrow \frac{\|\mathbf{u}^t - \mathbf{u}^k\|_{L^2}}{\|\mathbf{u}^t\|_{L^2}}$;
- 9 **if** $\eta_b < \eta_0^b$ **then**
- 10 $u_b \leftarrow u_k(x)$ for $x \in \Omega$ and $dist(x, \partial\Omega) = d$;
- 11 $\sigma \leftarrow \sigma_k$;
- 12 **break**;
- 13 **end**
- 14 Update σ_k with LM-CEM;
- 15 $norm \leftarrow \|\tau_k\|_{L_2}$;
- 16 $num \leftarrow num + 1$;
- 17 **end**
- 18 Reconstruct \mathcal{E}^δ from u_b in domain $\Omega' = \{x \mid x \in \Omega, dist(x, \partial\Omega) > d\}$;
- 19 $\sigma_k \leftarrow \sigma$;
- 20 $num \leftarrow 1$;
- 21 $norm \leftarrow 1$;
- 22 **while** $norm > \delta$ and $num < N_d$ **do**
- 23 Update u_k from σ_k with DCM;
- 24 Update σ_k with LM-DCM;
- 25 $norm \leftarrow \|\tau_k\|_{L_2}$;
- 26 $num \leftarrow num + 1$;
- 27 **end**

4. Numerical investigation

4.1. Phantom preparation and numerical setup

The variational forms of the linear systems defined by equations (27) in Section 3 can easily be obtained through integration by parts. They are solved with a mixed finite element method [31] which is implemented using FEniCS [32]. To illustrate the stability and accuracy of the presented approaches we the focus on numerical examples in a 2-dimensional (2D) problem. Two phantoms are considered.

The first example is a heart-lung model [33], see Figure 1a. The considered three tissues are heart (red, $\sigma = 0.7$ S/m), lung (cyan, $\sigma = 0.26$ S/m), and soft-tissues (blue, $\sigma = 0.33$ S/m). The model is placed into a circular region with a background material (white, $\sigma = 0.22$ S/m) and a radius $r = 25$ cm. The second example is the human brain model shown in Figure 1b. The considered tissues in this model include scalp (green, $\sigma = 0.5232$ S/m), skull (blue, $\sigma = 0.2923$ S/m), cerebro-spinal fluid (red, $\sigma = 2.1143$ S/m), gray matter (yellow, $\sigma = 0.5595$ S/m) and white matter (cyan, $\sigma = 0.3240$ S/m). Refer to [34] for conductivities of different tissues. The shape of this model is close to an ellipse whose semi-major and semi-minor axes are 6 cm and 7 cm. The model is placed in an ellipse region with a background material (white, $\sigma = 0.4$ S/m). The semi-minor and semi-major axes of the region are 8 cm and 9 cm, respectively. The conductivity maps



Figure 1: The 2D (a) heart-lung model and (b) human brain model embedded in a background material with electrodes (red squares) attached to the boundary (the solid black line). Different regions are marked with different colors. In (a), there are heart (red, $\sigma = 0.7$ S/m), lung (cyan, $\sigma = 0.26$ S/m), soft-tissues (blue, $\sigma = 0.33$ S/m), and background material (white, $\sigma = 0.22$ S/m). In (b), there are scalp (green, $\sigma = 0.5232$ S/m), skull (blue, $\sigma = 0.2923$ S/m), cerebro-spinal fluid (red, $\sigma = 2.1143$ S/m), gray matter (yellow, $\sigma = 0.5595$ S/m), white matter (cyan, $\sigma = 0.3240$ S/m) and the background material (white, $\sigma = 0.4$ S/m). All electrodes are uniformly distributed with the same corresponding central section angle. It is assumed that the electrical conductivity σ in the region close to boundary (between solid and dashed black lines) is known.

for the phantoms are piece-wise constant functions which will be mollified with

$$\eta_\epsilon(x, y) = C \exp\left(\frac{\epsilon^2}{(x^2 + y^2) - \epsilon^2}\right) \quad (28)$$

to produce $\sigma \in H^s(\Omega)$ with $s = 2$ for 2D problem. The constant $C > 0$ is selected so that $\int_{\mathbb{R}^2} \eta_\epsilon = 1$. The value of ϵ is 1 cm and 0.06 cm for heart-lung model and human-brain model, respectively. The true smoothed distributions of σ for the two models are shown in Figure 2.

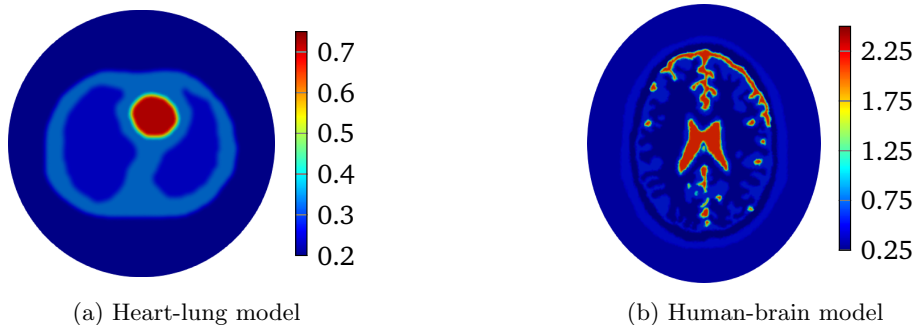


Figure 2: The true distribution of σ (a) for the 2D heart-lung model shown in Figure 1a and (b) for the 2D human brain model shown in Figure 1b

To work with CEM and LM-SCEM, 16 electrodes (red rectangles shown in Figure 1) are uniformly attached on the boundary (solid black lines). The section occupied by each electrode has the same central angle in both the heart-lung and human-brain models. The following computations assume that the conductivity in a small region close to boundary (between solid and dashed black lines) is known. The distance between the solid and dashed lines is given by δ_d . This known region helps to improve the convergence of the algorithm. Three current patterns based on Fourier basis functions are used in the computations, which are $I_l^{(n)} = \cos(n\theta_l)$ for $n = 1, 2, 3$, and $\theta_l = 2\pi l/L$. The regularization parameter α_k is chosen to decrease exponentially, and $\alpha_k = \alpha_0/a^k$ with $a > 1$. In what follows, a relatively large value is given to α_0 , and a value close to 1 is given to a for a slow decreasing of α_k to ensure the convergence of the iterations.

4.2. Performance of LM-SCEM

Numerical experiments on heart-lung model are carried out here to investigate the performance of LM-SCEM. A mesh of the circular domain with 77101 triangles is used for the reconstruction. The power density for each current pattern is simulated with CEM, and Gaussian white noise is added to avoid an inverse crime. Here, the noise level is measure with signal to noise ratio (SNR) $\text{SNR} = 20 \log_{10} \frac{\|\mathcal{E}_p\|_{L_2}}{\|\mathcal{N}\|_{L_2}}$, where \mathcal{N} is a Gaussian white noise distribution. The Levenberg-Marquardt iteration is stopped when $\|\tau\|_{L_2} < 1 \times 10^{-4}$ or total number of iterations greater than 15. These values were chosen to balance the quality in the reconstructions versus the computational speed. The reconstruction with different current patterns and different level of noise are considered to check the convergence of σ_k and the stability of LM-SCEM. The parameters for the reconstruction are given as $\alpha_0 = 50$, $a = 1.2$, and $\beta = 1.2 \times 10^{-3}$. These parameters are chosen to ensure that the reconstruction with current pattern $I^{(2)}$ converges. Other measurements are taken into the reconstruction without changing the parameters.

To simulate the power density $\mathcal{E}(\sigma)$, SCEM is used to yield better regularity of the electrical potential. The electrode conductance ζ_l of e_l is chosen as

$$\zeta_l(x) = \frac{1}{\epsilon^2} \exp\left(\frac{\epsilon^2}{x^2 - \epsilon^2}\right), \quad -\frac{l_e}{2} < x < \frac{l_e}{2}, \quad \epsilon = \frac{l_e}{2}, \quad l = 1, 2, \dots, L. \quad (29)$$

Here, l_e is the length of the electrode, which is proportional to the central angle corresponding to the electrode. $\zeta_l(x)$ is then scaled to have the required maximum value. The distribution of $\zeta_l(x)$ for the calculation in this paper is given in Figure 3a with a maximum value 1. The power density simulated with SCEM is given in Figure 3b for a region near one electrode. Here, the current pattern is $I^{(2)}$. A smooth distribution of $\mathcal{E}(\sigma)$ near the edge of the electrode is observed. For the same region, the power density simulated from CEM is also given in Figure 3c with $z_l = 2.0/\max \zeta(x) = 2\text{S/m}$ for $l = 1, 2, \dots, L$. Two singularity points are observed at the edges of the electrode. These singularities will cause instability in the reconstruction, and therefore SCEM is used in LM-SCEM.

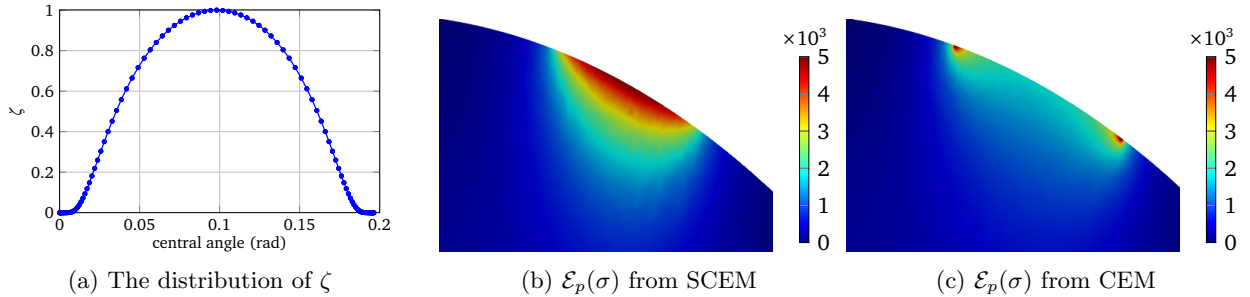


Figure 3: (a) The distribution of ζ on each electrode. (b) The power density $\mathcal{E}_p(\sigma)$ calculated from SCEM with the distribution of ζ given in (a). (c) The power density $\mathcal{E}_p(\sigma)$ calculated from CEM with $z_l = \frac{2}{\max \zeta}$

The LM-SCEM algorithm is used to reconstruct the distribution of σ . The initial guess is given as $\sigma_0 = 0.22\text{ S/m}$ which is the value of the background tissue. The conductivity in the region $x^2 + y^2 > (r - \delta_d)^2$ for $(x, y) \in \Omega$ is supposed to be known. The values of τ_k are truncated to only update $x^2 + y^2 \leq (r - \delta_d)^2$ for $(x, y) \in \Omega$ with $\delta_d = 4.5\text{ cm}$. The discontinuity caused by this truncation can be removed by applying (28) properly (either by mollification or simply by replacing the discontinuous values), but it does not cause any numerical problems since $\|\tau\|_k$ is small, so no special treatment was done in the following computation. The values of $\|\tau\|_{L_2}$ for the first 15 iterations are shown in Figure 4a. The relative error η is also given in Figure 4b. With 60 dB noise, the reconstruction with $I^{(2)}$ uniformly converges to $\eta = 3.08\%$ with 15 iterations. The reconstructed σ is shown in Figure 5a. To achieve a level of $\eta = 0.1\%$, it takes more than 40 iterations. A reconstruction with $I^{(2)}$ and $I^{(3)}$ is then carried out, but a similar speed of convergence and relative error is observed, result is in Figure 5b. When the current pattern $I^{(1)}$ is further considered into the reconstruction, an obvious improvement of convergence is seen, and a relative error level $\eta = 0.162\%$

is achieved with 14 iterations, the conductivity map is shown in Figure 5c. Therefore, the convergence of LM-SCEM depends not only on the regularization parameter α_k and the scaling parameter β , but also on the current patterns for the measurements. Since SNR = 60 dB indicates 0.1% of Gaussian noise in the simulated \mathcal{E}_p , the reconstructed result with $\eta = 0.162\%$ is already good, and more iterations will not improve the result. To verify, a reconstruction with $I^{(1)}$, $I^{(2)}$ and $I^{(3)}$ is carried out with SNR = 40 dB (1% noise). Relative errors are shown in Figure 4b, the reconstruction converges to $\eta = 0.973\%$ within 7 iterations, and more iterations did not bring any improvements. The reconstructed result is given in Figure 5d.

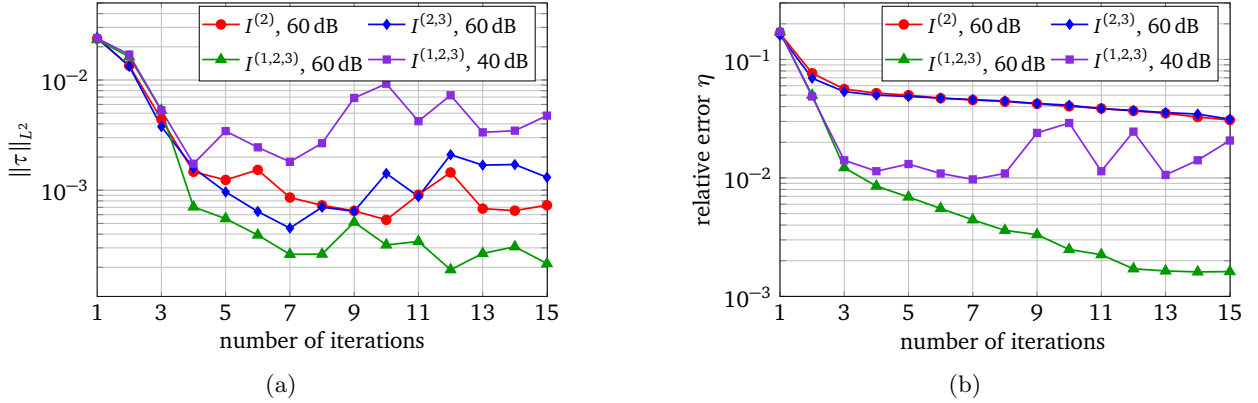


Figure 4: (a) The variation of $\|\tau_k\|_{L_2}$. (b) The relative error η of the reconstruction. With 60 dB noise, a uniform convergence is observed. With 40 dB noise, the reconstruction almost uniformly converges to $\eta = 0.973\%$ with 7 steps.

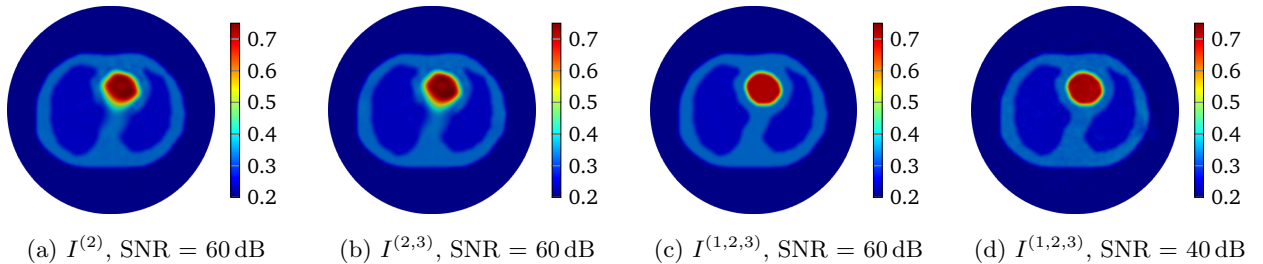


Figure 5: The conductivity map reconstructed from LM-SCEM with current pattern (a) $I^{(2)}$ with 60 dB noise, (b) $I^{(2,3)}$ with 60 dB noise, (c) $I^{(1,2,3)}$ with 60 dB noise, and (d) $I^{(1,2,3)}$ with 40 dB noise.

4.3. Performance of the mixed reconstruction approach

Though LM-SCEM performs well for reconstructing the conductivity map, its efficiency of the computation decreases quickly with the increase of measurements. Since EIT is not very sensitive to the change of interior conductivity, the electrical potential should converge faster than the convergence of the conductivity. The human-brain model is used here for numerical experiments with LM-SCEM. The elliptic domain is characterized with 8 cm major and 9 cm minor axes, and the domain is meshed with 36893 triangular elements. The parameters are given as $\alpha_0 = 150$, $a = 2.0$ and $\beta = 1 \times 10^{-3}$. The current patterns $I^{(2)}$ and $I^{(3)}$ are used in the reconstruction. With 60 dB noise, the iteration is terminated when $\|\tau\|_{L^2} < 1 \times 10^{-4}$ or the maximum number of iterations equals 30. The reconstruction based on LM-SCEM is shown in Figure 7a. \mathbf{U}^k of each current pattern is computed with SCEM and σ_k for k -th iteration, η^b easily follows then. The variation of the relative error η and η^b are shown in Figure 6a and Figure 6b, respectively. As can be seen, η slowly converges to 4.09%. This error is much larger than the input noise level, this is mainly caused by the complexity of the phantom and the high contrast of σ among different tissues. But the potentials on the boundary for both $I^{(2)}$ and $I^{(3)}$ converge fast to a level of $\eta^b < 1 \times 10^{-4}$ in few iterations. Therefore, the

boundary potential converges much faster. This property is exploited here to accelerate the computation by mixing LM-SCEM and LM-DCM, as demonstrated in Algorithm 2. In this computation, the LM-SCEM is stopped when η^b for all current patterns are smaller than 1×10^{-3} . The LM-DCM is performed in the region $\Omega' = \{x \mid x \in \Omega, \text{dist}(x, \partial\Omega) > 5 \text{ mm}\}$ with $\delta_d = 5 \text{ mm}$. The potential on $\partial\Omega'$ is computed with SCEM and the reconstructed σ from LM-SCEM. The power density in Ω' can be reconstructed with the method introduced by Ammari *et al* [4]. However, it requires the knowledge on the deformation caused by the ultrasonic waves, therefore, we compute it with DCM instead. Noise with SNR= 60 dB is added, and LM-DCM is used for the reconstruction. The relative error η is given in Figure 6a. The conductivity map is reconstructed with $\eta = 8.13 \times 10^{-4}$ in 30 iterations, and the result is given in Figure 7b. Here, the time required for 30 LM-DCM iterations is about 20 minutes which is approximately the time needed for one LM-SCEM iteration. So the reconstruction efficiency is greatly improved, and better results are obtained. A similar computation with 40 dB noise is further considered here. As seen in Figure 6b, increasing noise does not influence much the convergence of the boundary potential, therefore, this mixed approach can be a good way to remove noise from the measured power density. With 40dB noise in the reconstructed power density in Ω' , the distribution of σ obtained with LM-DCM is shown in Figure 7d. Comparing it to the results obtained with LM-SCEM, as shown in Figure 7c, a better noise tolerance is observed in LM-DCM.

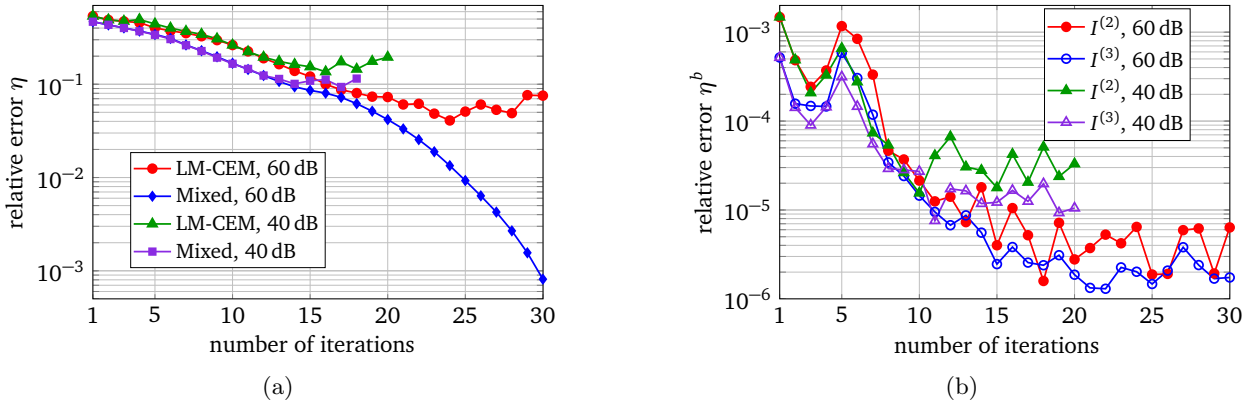


Figure 6: (a) The relative error η of different reconstructions. (b) The convergence of the boundary potential for LM-CEM with different level of noise.

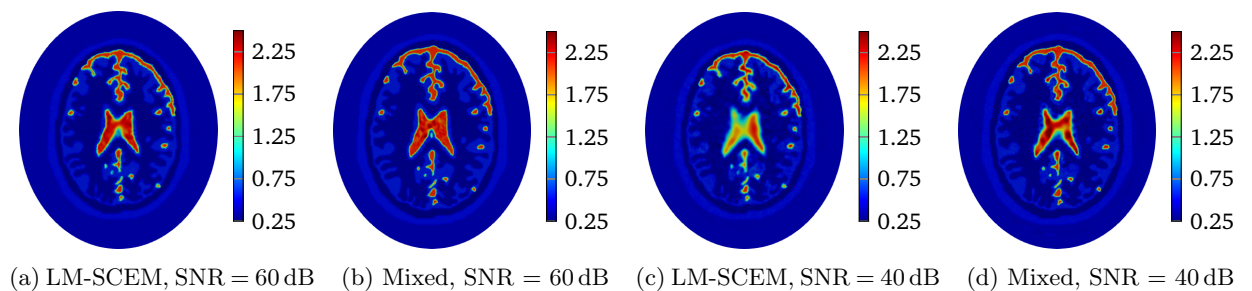


Figure 7: The conductivity map of human-brain model reconstructed with current pattern $I^{(2)}$ and $I^{(3)}$. The reconstruction with only LM-CEM are given in (a) and (c) for 60 dB and 40 dB noises. Corresponding reconstructions by mixing LM-SCEM and LM-DCM are given in (b) and (d).

5. Conclusion

The work first developed a computational approach for AET by incorporating CEM into the Levenberg-Marquardt algorithm. Since the regularity of the power density obtained with traditional CEM is limited

because of the Robin-type discontinues boundary conditions, a recently proposed smoothed CEM is used in this paper. Numerical investigation shows that this iterative method can stably reconstruct the conductivity map of complex phantoms, and a good accuracy can be achieved even with a certain level of noise though this also depends on the current patterns used in the measurements.

However, the reconstruction algorithm becomes inefficient quickly when the number of measurements is increased. Since EIT is not very sensitive to the changes of the internal conductivity, the boundary potential converges to its true value much faster than the convergence of the conductivity. This fact is then used to build a mixed computational approach. LM-SCEM is used to reconstruct the boundary potentials in a few iterations, and LM-DCM is applied to reconstruct the conductivity distribution based on the obtained boundary potential. It is observed in the given example that the time for one LM-SCEM iteration is enough for the whole calculation of LM-DCM, so the reconstruction efficiency is greatly improved with the mixed strategy.

Here, reconstruction with LM-DCM requires a first step to compute the power density from the obtained boundary potential from LM-SCEM. This additional step can be considered as a step to smooth the electrical potential and to remove the noise in the measured power density, in addition to the better noise tolerance of LM-DCM compared to LM-SCEM, a better reconstruction can be obtained with the mixed algorithm.

Several numerical experiments are carried out with a heart-lung phantom and a complex human brain model. The performance of the presented reconstruction approaches are well demonstrated with different number of measurements. The proposed method applies also to 3-dimensional acousto-electric tomography and anisotropic conductivity distributions; we leave the implementation in these scenarios for future work.

Acknowledgement

The majority of the work was done while Changyou Li was postdoc at the Department of Applied Mathematics and Computer Science, Technical University of Denmark in 2018. We thank the Danish Council for Independent Research — Natural Sciences (grant 4002-00123) for financial support.

References

- [1] D. S. Holder, *Electrical impedance tomography* ;, IOP Press,, 2005 (2005).
- [2] T. J. Yorkey, *Electrical impedance tomography with piecewise polynomial conductivities*, *Journal of Computational Physics* 91 (1990) 344 – 360 (1990).
- [3] A.-P. Calderón, *On an inverse boundary value problem*, in: *Seminar on Numerical Analysis and its Applications to Continuum Physics (Rio de Janeiro, 1980)*, Soc. Brasil. Mat., Rio de Janeiro, 1980, pp. 65–73 (1980).
- [4] H. Ammari, E. Bonnetier, Y. Capdeboscq, M. Tanter, M. Fink, *Electrical impedance tomography by elastic deformation*, *SIAM Journal on Applied Mathematics* 68 (2008) 1557–1573 (2008).
- [5] G. Uhlmann, *Electrical impedance tomography and Calderón’s problem*, *Inverse Problems* 25 (2009) 123011 (2009).
- [6] B. Brown, *Electrical impedance tomography (EIT): a review*, *Journal of Medical Engineering and Technology* 27 (2009) 97–108 (2009).
- [7] D. K. Han, A. Prosperetti, *A shape decomposition technique in electrical impedance tomography*, *Journal of Computational Physics* 155 (1999) 75 – 95 (1999).
- [8] C.-T. Hsiao, G. Chahine, N. Gumerov, *Application of a hybrid genetic/powell algorithm and a boundary element method to electrical impedance tomography*, *Journal of Computational Physics* 173 (2001) 433 – 454 (2001).
- [9] E. T. Chung, T. F. Chan, X.-C. Tai, *Electrical impedance tomography using level set representation and total variational regularization*, *Journal of Computational Physics* 205 (2005) 357 – 372 (2005).
- [10] K. Knudsen, M. Lassas, J. Mueller, S. Siltanen, *Regularized d-bar method for the inverse conductivity problem*, *Inverse Problems and Imaging* 3 (2009) 599–624 (2009).
- [11] H. Ammari, *An Introduction to Mathematics of Emerging Biomedical Imaging*, 1st Edition, *Mathématiques et Applications*, Springer-Verlag Berlin Heidelberg, 2008 (2008).
- [12] G. Bal, *Hybrid inverse problems and internal functionals*, in: *Inverse Problems and Applications: Inside Out II*, MSRI Publications, 2012, pp. 325–368 (2012).
- [13] P. Kuchment, *Mathematics of hybrid imaging: A brief review*, in: *The Mathematical Legacy of Leon Ehrenpreis*, Springer Milan, Milano, 2012, pp. 183–208 (2012).
- [14] D. B. Geselowitz, *An application of electrocardiographic lead theory to impedance plethysmography*, *IEEE Transactions on Biomedical Engineering BME-18 (1971) 38–41 (1971)*.
- [15] J. Jossinet, B. Lavandier, D. Cathignol, *Impedance modulation by pulsed ultrasound*, *Ann. N. Y. Acad. Sci.* 873 (1999) 396–407 (1999).

- [16] J. Jossinet, C. Trillaud, S. Chesnais, Impedance changes in liver tissue exposed in vitro to high-energy ultrasound, *Physiological Measurement* 26 (2005) S49–S58 (2005).
- [17] B. C. S. Jensen, A. Kirkeby, K. Knudsen, Feasibility of acousto-electric tomography – a numerical study, in preparation (2019).
- [18] X. Song, Y. Xu, F. Dong, Linearized image reconstruction method for ultrasound modulated electrical impedance tomography based on power density distribution, *Measurement Science and Technology* 28 (4) (2017) 045404 (2017).
- [19] X. Song, Y. Xu, F. Dong, Sensitivity matrix for ultrasound modulated electrical impedance tomography, in: 2016 IEEE International Instrumentation and Measurement Technology Conference Proceedings, 2016, pp. 1–6 (May 2016).
- [20] G. Bal, W. Naetar, O. Scherzer, J. Schotland, The Levenberg-Marquardt iteration for numerical inversion of the power density operator, *Journal of Inverse and Ill-posed Problems* 21 (2013) 265–280 (2013).
- [21] B. J. Adesokan, K. Knudsen, V. P. Krishnan, S. Roy, A fully non-linear optimization approach to acousto-electric tomography, *Inverse Problems* 34 (10) (2018) 104004, 16 (2018). doi:10.1088/1361-6420/aad6b1. URL <https://doi-org.proxy.findit.dtu.dk/10.1088/1361-6420/aad6b1>
- [22] B. C. S. Jensen, K. Knudsen, B. Jin, B. J. Adesokan, Acousto-electric tomography with total variation regularization, *Inverse Problems* (2018). doi:10.1088/1361-6420/aaece5.
- [23] S. Roy, A. Borzi, A new optimization approach to sparse reconstruction of log-conductivity in acousto-electric tomography, *Siam Journal on Imaging Sciences* 11 (2) (2018) 1759–1784 (2018). doi:10.1137/17m1148451.
- [24] M. Gupta, R. K. Mishra, S. Roy, Sparse reconstruction of log-conductivity in current density impedance tomography, *Journal of Mathematical Imaging and Vision* (2019) 1–17 (2019). doi:10.1007/s10851-019-00929-5.
- [25] S. Hubmer, K. Knudsen, C. Li, E. Sherina, Limited-angle acousto-electrical tomography, *Inverse Problems in Science and Engineering* (2018) 1–20 (2018). doi:10.1080/17415977.2018.1512983.
- [26] E. Somersalo, M. Cheney, D. Isaacson, Existence and uniqueness for electrode models for electric current computed tomography, *SIAM Journal on Applied Mathematics* 52 (1992) 1023–1040 (1992).
- [27] N. Hyvönen, L. Mustonen, Smoothed complete electrode model, *ArXiv e-prints* (Mar. 2017). arXiv:1703.08022.
- [28] B. Kaltenbacher, A. Neubauer, O. Scherzer, *Iterative Regularization Methods for Nonlinear Ill-Posed Problems*, Berlin, Boston: De Gruyter, 2008 (2008).
- [29] A. Lechleiter, A. Rieder, Newton regularizations for impedance tomography: Convergence by local injectivity, *Inverse Problems* 24 (6) (2008) 065009 (2008). doi:10.1088/0266-5611/24/6/065009.
- [30] E. Kreyszig, *Introductory Functional Analysis with Applications*, John Wiley & Sons, New York, 1978 (1978).
- [31] D. Boffi, F. Brezzi, M. Fortin, *Mixed Finite Element Methods and Applications*, Springer Berlin Heidelberg, 2013 (2013).
- [32] M. S. Alnæs, J. Blechta, J. Hake, A. Johansson, B. Kehlet, A. Logg, C. Richardson, J. Ring, M. E. Rognes, G. N. Wells, The fenics project version 1.5, *Archive of Numerical Software* 3 (100) (2015).
- [33] S. Zlochiver, M. Rosenfeld, S. Abboud, Induced-current electrical impedance tomography: a 2-D theoretical simulation, *IEEE Transactions on Medical Imaging* 22 (2003) 1550–1560 (2003).
- [34] D. Andreuccetti, R. Fossi, C. Petrucci, An internet resource for the calculation of the dielectric properties of body tissues in the frequency range 10 Hz - 100 GHz, based on data published by C.Gabriel et al. in 1996. (1997). URL <http://niremf.ifac.cnr.it/tissprop/>